Analysis of iron-chromium-aluminum samples exposed to accident conditions followed by quench in the QUENCH-19 experiment

Peter Doyle[a,*], Juri Stuckert[b], Mirco Grosse[b], Martin Steinbrück[b], Andrew T. Nelson[a], Jason Harp[a], Kurt Terrani[a]

[a] *Nuclear Fuel and Energy Cycle Division, Oak Ridge National Laboratory, TN, USA*
[b] *Institute for Applied Materials, Karlsruhe Institute of Technology, Eggenstein-Leopoldshafen, Germany*

ARTICLE INFO

Keywords:
QUENCH
ATF
FeCrAl
B136Y3
Beyond design basis
Accident-tolerant

ABSTRACT

The QUENCH-19 experiment was a first-of-its-kind full-bundle test simulating accident conditions followed by water quench on accident-tolerant fuel (ATF) cladding. A type of FeCrAl(Y) alloy, B136Y3, was developed at Oak Ridge National Laboratory and tested at the Karlsruhe Institute of Technology using Kanthal APM corner rods, a shroud, and Kanthal AF spacer grids. Testing conditions were similar to those in QUENCH-15—which tested ZIRLO cladding behavior—so that B136Y3 and ZIRLO cladding could be compared. QUENCH-19 consisted of an initial pre-oxidation heating followed by a transient. Then, a maximum power hold, which was not present in QUENCH-15, was executed to extend the heating period for the FeCrAl(Y) rods. Finally, a rapid water quench was executed that was similar to emergency core coolant system (ECCS) actuation. Compared with the ZIRLO rods in QUENCH-15, the bundle in QUENCH-19 released significantly less H_2 (9.2 g vs. 47.6 g) and achieved a much lower maximum temperature (1455°C vs. 1880°C). Furthermore, no breakaway oxidation was observed in QUENCH-19. Metallographic mounts revealed that despite the symmetry of the setup, at elevations near the maximum temperature, cladding and thermocouples were heavily damaged, substantial melting and oxidation occurred, and the cladding underwent chemical interaction with the thermocouple sheaths. Additionally, the ZrO_2 spacers detrimentally interacted with the cladding, leading to mixed oxide debris and the full destruction of some rods. Additional failure was found in certain cooler rods that may have risen due to the high thermal expansion coefficient of FeCrAl alloys. This paper presents an analysis of this work, which suggests that FeCrAl cladding can chemically survive anticipated loss-of-coolant accident events followed by rapid ECCS quench if the correct geometry and core design are present.

1. Introduction

The QUENCH series of tests was originally designed to test the performance of Zr-based alloys under accident conditions followed by a rapid water quench [1–8]. These tests revealed useful information about the release of H_2 and initial temperature increases as a function of a variety of parameters. As the industry has sought more accident-tolerant fuels (ATF) since the Fukushima Daiichi accident in 2011, materials such as SiC, FeCrAl, and Cr-coated Zr alloys have gained increasing attention, partly because of their excellent oxidation properties under accident scenarios [9–17]. Testing candidate ATF cladding materials under representative high-temperature steam oxidation conditions remains an important step in developing these materials, but experience has shown that material response to the transient oxidization conditions following emergency core coolant system (ECCS) actuation is more complicated to predict.

Previous QUENCH tests [2,6,18] have shown that when quenching from high temperatures, the sudden impact of water onto the hot rods can lead to a significant oxidation of the material that releases energy and H_2, causing a temporary temperature escalation before additional cold water reduces the temperature and minimizes further oxidation. In Zr-based alloys, this temperature escalation can result in the partial melting of claddings, as reported for ZIRLO in QUENCH-15 [18], or to oxide spalling (i.e., breakaway), as reported for the E-110 Zr alloy in QUENCH-12 [19]. To understand the thermal and chemical behavior of ATF cladding under such accident conditions and to determine the microstructural effects, QUENCH-19 was performed using an Oak Ridge National Laboratory (ORNL) FeCrAl alloy, B136Y3.

This paper summarizes the QUENCH-19 test conditions and results. Metallographic post-test examinations of the FeCrAl are pre-

* Corresponding author.
E-mail address: pdoyle3@vols.utk.edu (P. Doyle).

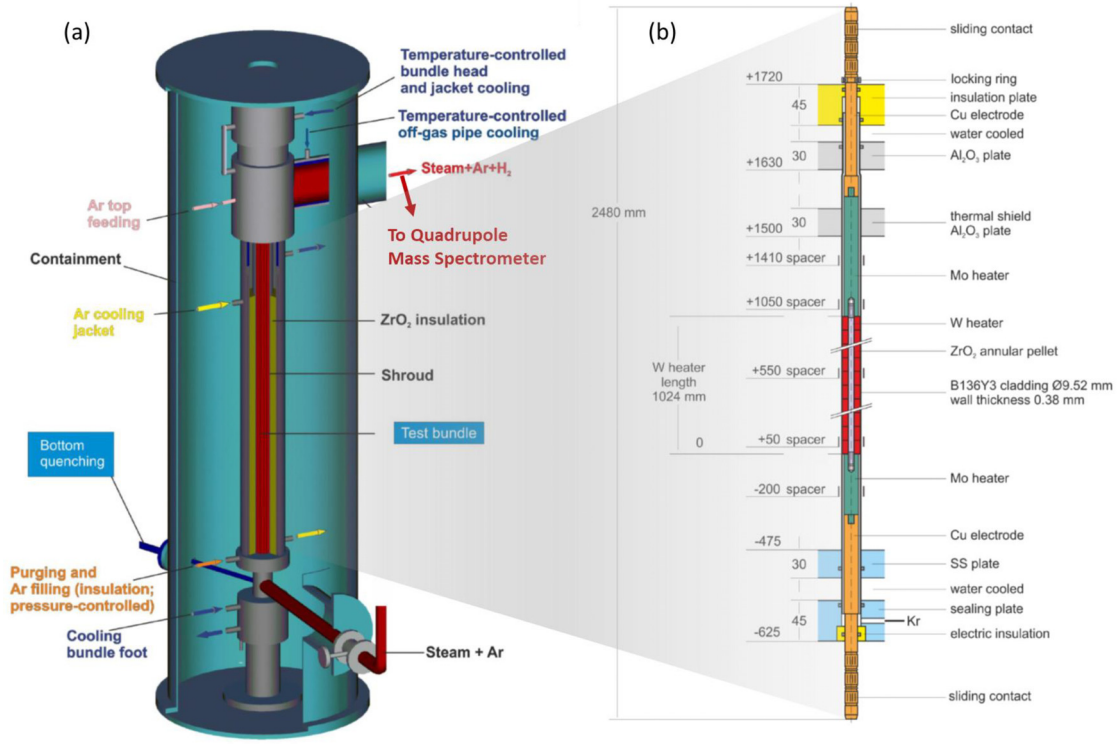

Fig. 1. Schematics of (a) the QUENCH test chamber and bundle assembly showing cooling lines and experiment gas flows and (b) simulant fuel rod. The Kr channel is shown at the base of the rod diagram.

sented and analyzed in the context of the response of a light-water reactor core using FeCrAl cladding to a loss-of-coolant accident (LOCA) and ECCS quench.

2. Materials and methods

2.1. Test configuration and materials

The QUENCH-19 test was conducted in forced convection mode at the QUENCH facility, where Ar was combined with super-heated steam at a specific rate through the bundle to simulate an LOCA. The mixture passed through the bottom of the bundle and out the top and was sampled by a Balzers GAM 300 quadrupole mass spectrometer continuously throughout the test, see Fig. 1(a). The mass spectrometer allowed the H_2 release rate to be determined. System absolute pressure was maintained at approximately 0.2 MPa.

The hydraulic diameter of the system was 12.27 mm, the grid pitch was 12.6 mm, and the coolant channel area was 34.57 cm^2. Each rod was composed of central tungsten heating elements, 1024 mm long and 5 mm in diameter. Each tungsten segment was connected to Mo heater rods that were coupled to Cu electrodes, as shown in Fig. 2.

During the test, heating was accomplished with an external DC power supply. Eleven millimeter long, 5% yttria-stabilized zirconia annular pellets with 8.6 mm outer diameters and 5.2 mm inner diameters were stacked around the tungsten heaters to serve as thermal surrogates for UO_2 fuel. Around these pellets was fixed a cold-drawn $Fe_{bal}Cr_{13}Al_{6.2}Y_{0.03}C_{0.01}$ cladding (i.e., B136Y3) from ORNL. The cladding was 381 ± 9 μm thick and had an outer diameter of 9.52 ± 0.04 mm and an inner diameter of 8.76 ± 0.04 mm. Similar to the reference test, QUENCH-15, once the peak rod temperature reached 523°C, the rods were filled with Kr to a pressure of 0.23 MPa. As in all previous bundle tests, ballooning and burst phenomena were not modeled here, since the main goal was to study the effects of cladding oxidation. All rods were connected by gas communication channels to a Kr reservoir. The common reservoir made it possible to easily detect initial rod failure and the progression of failure by observing Kr in the outlet gas stream. However, this reservoir decreased the chance of cladding balloon and burst events. Additional tests which can evaluate balloon and burst are reserved for future work.

In addition to the test rods, seven corner rods were installed in the system and labeled A–G. Their positions are shown in Fig. 2(a). Four of the corner rods—A, C, E, and G—were divided into two sections. The top sections were made of solid 6 mm diameter Kanthal APM ($Fe_{bal}Cr_{22}Al_{5.8}Si_{0.7}Mn_{0.4}C_{0.08}$) rods, and the bottom sections were 6 mm outer diameter Kanthal D tubes, each with a 0.4 mm wall thickness. The bottom tube sections were used for thermocouple instrumentation. Fully solid Kanthal APM rods B, D, and F were used for oxide thickness measurements at three points during the test, as in QUENCH-15 [2,8,18]. Rod B was withdrawn after the pre-oxidation, F was withdrawn after the transient, and D was withdrawn after the test. Solid rods were used for oxide thickness measurements as it maximizes the material available for oxidation. In former QUENCH tests, thick oxide layers were formed on Zr-based rods [18]. Furthermore, oxidized solid rods are stiffer and less prone to fracture than oxidized tubes, which is important when they are pulled out of the bundle during the experiment.

All rods were held in place by five spacer grids, as shown in Fig. 1(b). The low-temperature grid, a standard AREVA Inconel grid, was located at −200 mm (0 mm was defined as the bottom of the tungsten heater element), and the four grids in the heated section were ORNL Kanthal AF grids. Besides friction with the spacer grids, axial motion of the rods was not constrained, similar to actual commercial operation. The sliding contacts on each end of the rod provided for any needed rod axial motion while allowing continuous electrical contact to the tungsten surrogate heating elements. These gold-plated contacts are a set of axial lamellas that perform a role similar to spring elements in spacer grids. During assembly, thermocouples on the test rods were welded on the test rod

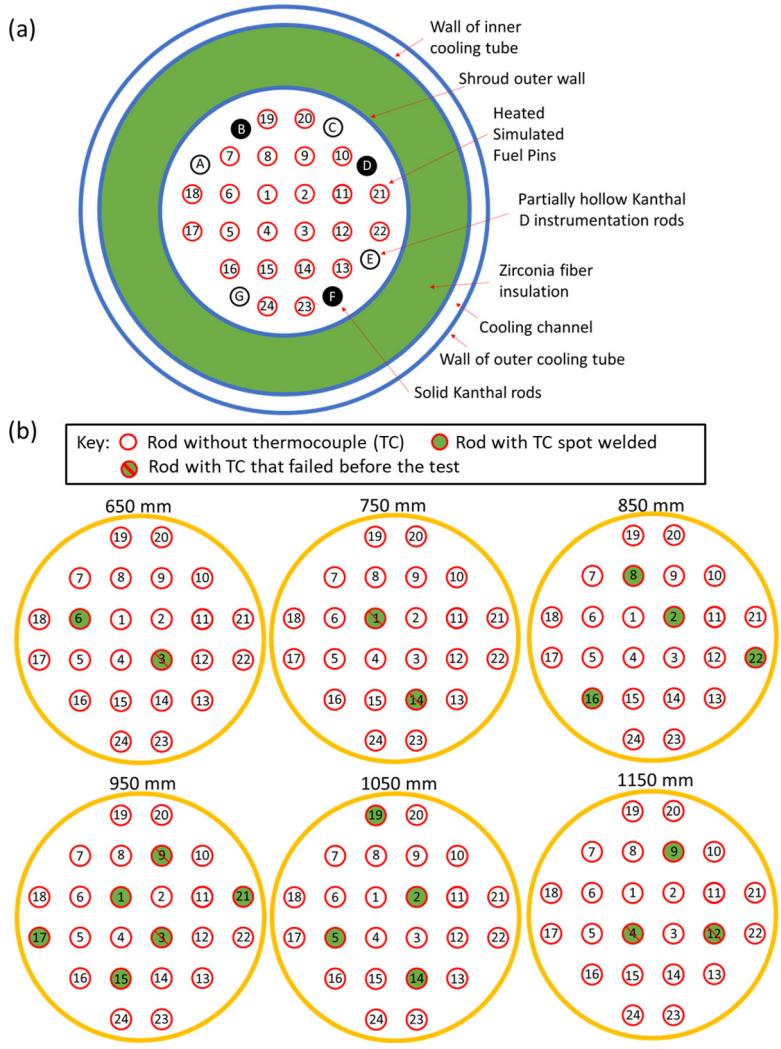

Fig. 2. (a) A generic cross section diagram shows the configuration of the rods and their labeling conventions together with the shroud, shroud insulation, and coolant channel walls. Corner rods A, C, E, and G are shown as unshaded circles. The other three rods—B, D, and F—are shown as solid circles. (b) Axial thermocouple (TC) locations on the cladding of the fuel simulant rods are shown between 650 and 1150 mm, which is the hot section of the test. A key differentiates between rods without TCs, with TCs that provided data, and rods whose TCs failed before the test.

cladding at the radial location farthest from the center of the bundle. Thermocouples at and below 850 mm were inserted from the base of the assembly, and the thermocouples above 850 mm were inserted from the top of the assembly. Thermocouple locations at different bundle heights are shown in Fig. 2(b). Some thermocouples failed before the test and no data are available from them. However, they are included because of interactions between thermocouple sheaths and the cladding.

Two different thermocouples were used in this test. Thermocouples in the hottest section (i.e., above 550 mm) were W5Re/W26Re, insulated by MgO, and sheathed with an American Iron and Steel Institute (AISI) 304 stainless steel tube with an outer diameter of 2.4 mm and wall thickness of 500 µm. Below 550 mm and for thermocouples outside of the shroud, NiCr/Ni thermocouples with MgO insulation and sheathed with 1 mm diameter AISI 304 stainless steel were used. Temperature, voltage, current, and pressure data were all collected at a rate of 1 Hz.

A Kanthal APM shroud was placed around the bundle assembly. This shroud was surrounded by 34 mm of ZrO_2 fiber insulation. Before the test, the annulus was filled with Ar after repeated evacuations to purge O_2. During the test, a purge/refill system maintained the pressure of the annulus at 0.23 MPa. A double-walled coolant channel was placed around the purge/refill system. Argon was continuously flowed through this channel from top to bottom to cool the test chamber exterior. Water was used as a coolant near the upper electrodes. This configuration is shown in Fig. 1(a).

2.2. Test conditions

Test conditions in QUENCH-19 were closely matched to those of QUENCH-15, in which ZIRLO cladding was tested with pre-oxidation, a transient, and a water quench. Before the quench stage, steam and Ar were injected at a rate of 3.8 and 3.5 g/s, respectively. Inlet gas temperature, measured by NiCr/Ni thermocouples at the inlet, was about 370°C at the start of the test and increased to about 430°C by the end of the pre-oxidation stage. QUENCH-15 was also run with 3.5 g/s Ar; however, steam was injected at a slower 3.2–3.4 g/s and was constantly maintained at about 450°C at the inlet, 20–50°C higher than QUENCH-19. The temperature was lower in QUENCH-19 because of a change in the pre-heater design, which occurred after the QUENCH-15 test. During pre-oxidation and the transient, the QUENCH-19 power profile mirrored the QUENCH-15 power profile almost exactly at about 11 kW for 6018 s, followed by a power transient that increased the power up to 18.3 kW over 1109 s. Unlike QUENCH-15, the power was then held at 18.3 kW for 1973 s. ATF cladding is de-

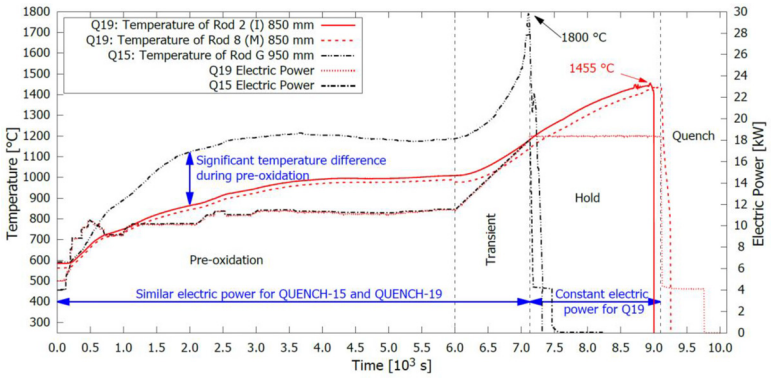

Fig. 3. Temperature and power profiles of QUENCH-19 and QUENCH-15 [18] as a function of test time. Electric power [kW] is shown on the *y2*-axis, temperature [°C] is shown on the *y*-axis, and each section of the test is labeled and separated by dashed vertical lines. The power is similar for both tests, excepting the intentional hold period for QUENCH-19. Maximum temperature in QUENCH-15 (at 950 mm) occurred due to strong oxidation during the transient and reflood, whereas the maximum of 1455°C in QUENCH-19 was achieved without significant oxidation. Adapted from J. Stuckert et al. [3].

signed specifically to provide additional response time in the event of an accident scenario. The additional power hold in QUENCH-19 simulated such an extended accident to evaluate the performance improvement that could be achieved over Zr-based alloys [14,20,21]. Finally, water was introduced at a rate of 48 g/s, similar to QUENCH-15.

2.3. Post-test evaluation

After the test, a videoscope was inserted into the assembly to take images of the resulting internal features. The entire assembly was then embedded in Epotec 277 epoxy resin hardened by Epikure 350. Initially, the resulting epoxy had no cracks or pores, and it was cut at 16 mm intervals for polishing and microscopy analysis. Because the epoxy was soft, mounts were placed in special holders during the polishing process. Despite these precautions, some cracks did form during processing. Metallographic mounts were then examined by scanning electron microscopy (SEM) and energy-dispersive spectroscopy (EDS) on a TESCAN MIRA3 instrument at ORNL, and on a FEI XL40 SFEG instrument at the Karlsruhe Institute of Technology (KIT).

3. Results

3.1. Comparison of system performance in QUENCH-15 and QUENCH-19

Although the power profile and test geometries were nearly identical for QUENCH-15 and QUENCH-19, as shown in Fig. 3, some dissimilarities existed. Section 2.2 notes that the inlet Ar/steam mixture in QUENCH-19 at the base of the bundle was cooler than in QUENCH-15 by up to 50°C, although in the transient and hold stages the difference between QUENCH-15 and QUENCH-19 was only about 20°C. Additionally, the two tests differed in shroud boundary conditions. Though both were designed for a dry Ar atmosphere and ZrO_2 insulated shroud annulus, in QUENCH-19 the shroud insulation was compromised by steam or water ingress through a gap defect at the upper flange of the shroud, which occurred during pre-tests of the system. The temperature increase during pre-oxidation led to boil-off of the ingress water, as found by temperature increases on the inner wall of the shroud. Boil-off at different locations occurred at different times ranging from approximately 2000 s at 850 mm elevation to approximately 6000 s at 350 mm. This maintained the temperature of the shroud annulus near the boiling point of water, 125°C at 0.23 MPa pressure [22], until after boil-off occurred, limiting initial thermal buildup in the test during pre-oxidation.

Argon was periodically injected to the base of the shroud to compensate for the loss of Ar and ingressed water as evaporated as steam during pre-oxidation. It was estimated that 320 g of water was lost by evaporation during the test, 7300 g drained out of the annulus during test disassembly, and 400 g remained trapped in insulation pores after the test, as indicated by insulation weight.

Thus, whereas the boundary conditions during the transient, hold, and quench portions of the test were similar to those of QUENCH-15, during pre-oxidation the QUENCH-19 test was not as well insulated, leading to lower heat retention. Consequently, QUENCH-19 was observed to have a greater radial heat distribution from the bundle center to exterior than QUENCH-15 (about 165°C, compared to about 120°C in QUENCH-15) during pre-oxidation, see Fig. 4 and Stuckert et al. [2,18].

In addition to this, FeCrAl alloy cladding, as currently planned, will require a larger fuel pellet and thinner cladding than currently used with conventional Zr-based cladding. As such, the ZrO_2 pellets in this work were slightly larger (OD = 8.6 mm) than in QUENCH-15 (OD = 8.2 mm). The combined effects of all factors related to geometry, boundary conditions, and cladding oxidation differences resulted in differences in bundle behavior during the pre-oxidation stage of the test. During pre-oxidation, the temperature in QUENCH-15 increased to around 1200°C after about 2500 s. QUENCH-19, by contrast, reached a lower peak pre-oxidation temperature of about 1000°C over a longer 3500 s.

Some of this temperature difference undoubtedly relates to the faster oxidation rate of ZIRLO compared to that of FeCrAl [9,14,23,24]. However, this is not expected to account for the significant temperature differential between QUENCH-15 and QUENCH-19. The amount of electrical energy added during pre-oxidation was 64 MJ in both tests, compared to only about 3.5 MJ of energy by oxidation of the cladding in QUENCH-15 [18]. Energy released by oxidation in QUENCH-19 was significantly lower, as indicated by substantially less hydrogen released during pre-oxidation, see Section 3.3.

3.2. Thermal history at 650–1150 mm

The hottest recorded temperatures are observed at 850 mm in QUENCH-19 and rather at 950 mm in QUENCH-15, and plotted in Figs. 3 and 4. Fig. 4 shows data from thermocouples that were available. Thermocouples were labeled as either interior ("I," corresponding to rods 1–4), middle ("M," corresponding to rods 5–16), or external ("E," corresponding to rods 17–24). Elevations are shown at 650–850 mm in Fig. 4(a), 950 mm in Fig. 4(b), and 1050–1150 mm in Fig. 4(c). Above and below these elevations, thermo-

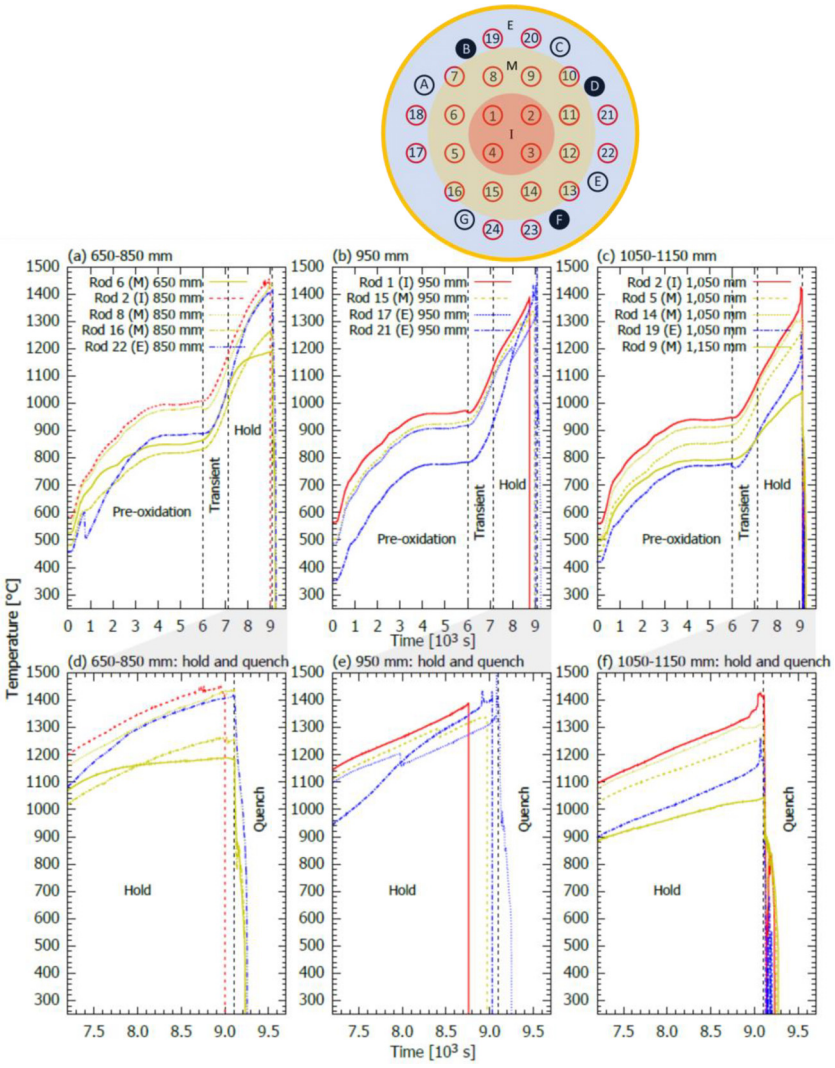

Fig. 4. Thermocouple readouts from QUENCH-19 across the elevation ranges (a) 650–850 mm, (b) 950 mm, and (c) 1050–1150 mm. (d), (e) and (f) show higher magnifications of the hold and quench portions of the test at the elevations in (a), (b), and (c), respectively. Each key entry includes a rod locator designation "(X)," where X is I, M, or E (representing one of the internal rods [#1–4], one of the midrange rods [#5–16], or one of the exterior rods [#17–24], respectively). Three ranges—pre-oxidation, transient, and hold—are identified and separated by dashed vertical lines on the plot and a rod diagram above the plot correlates shows the different regions, (I, M, and E) with the same colors as on the graphs.

couple readings were lower, as shown in Fig. 4 for elevations from 650 to 1050 mm.

However, a few caveats must be noted. First, as shown in Fig. 1(b), several thermocouples failed before the test began, preventing data from being collected at 750 mm and limiting available data at 950 mm. This includes one of the interior rod thermocouples at 950 mm, leaving only a single interior rod thermocouple on rod 1 at 950 mm. In addition, some of the remaining thermocouples also failed near the end of the hold period of the test, as shown in Fig. 4 (d–f), which show only the hold and quench portions of the test at the same elevations as those in Fig. 4(a–c), respectively. As shown in Fig. 4(d) and (e), three of the four thermocouples at 950 mm elevation and at 850 mm the rod 2 thermocouple failed just before the quench portion of the test. Therefore, it is possible that temperatures were higher at the conclusion of the test than measured, particularly in the center of the bundle and at 950 mm.

Second, the maximum stable temperature reported was 1455°C at 850 mm on rod 2, as shown in Fig. 4(a). Although this was the maximum consistent temperature, an exterior thermocouple on rod 17 at 950 mm survived to the end of the test and reported a single-point maximum of about 1520°C, which is significantly higher than the 1455°C reported stable maximum. However, the 1520°C reading is considered to be instrumental error because the thermocouple reported such a high temperature only once. The reported temperatures one second before and after the 1520°C reading were about 200 and 150°C lower, respectively. It is unlikely that the thermocouple would have heated 200°C in one second and cooled by 150°C in the next second.

With these caveats in mind, the temperature profiles in Fig. 4 show important features of the QUENCH-19 test. Fig. 4(a) and (d) show pre-hold partial similarity between the 650 mm and 850 mm elevations. In particular, the 650 mm thermocouple on rod 6 was within approximately 50°C of the similarly placed rod 16 at 850 mm until after the hold. After the hold, the 850 mm thermocouple increased to approximately 100°C hotter than the 650 mm thermocouple. However, on the other side of the bundle, external rod 22 at 850 mm was measured to have consistently higher temperatures than rod 16 at 850 mm. After the hold, the temperature of rod 22 at 850 mm increased to approximately 150°C hotter than rod 16. Furthermore, rod 8, a mid-range rod about one-fourth turn from both rods 22 and 16, had an almost

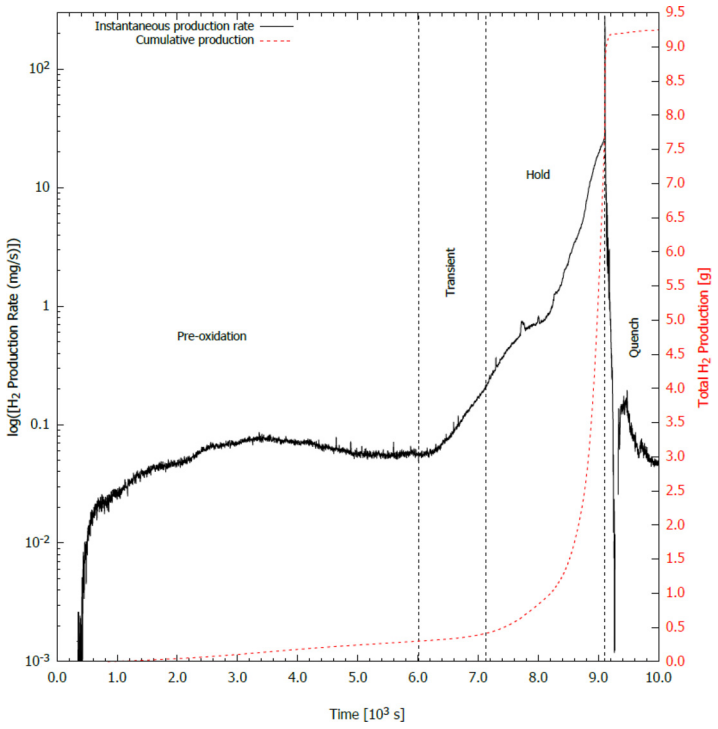

Fig. 5. Hydrogen generation rates in the QUENCH-19 test. Full test period showing instantaneous release, excluding the production spike (y-axis), and cumulative produced H_2 (second y-axis).

identical temperature profile to the internal rod 2 at 850 mm. The temperatures of rods 2 and 16 consistently tracked with the other 850 mm rods by 100–200°C, except after the hold when the temperature of external rod 22 increased to be nearly identical to the temperatures of rods 16 and 2.

Similar thermal asymmetry was observed at other elevations. As shown in Fig. 4(b) and (e), at 950 mm, external rods 17 and 21, again on opposite sides of the bundle, differed by about 100–200°C until after the transient, when rod 21's temperature increased rapidly and the thermocouple failed before the quench. Rod 17, by contrast, maintained a similar temperature to the internal and mid-range rods at 950 mm. Despite the single-point temperature spike previously discussed, rod 17 also remained fairly stable and survived the entire test. Thermocouples on rods 1 and 15 tracked closely throughout the test.

At 1050 mm, as shown in Fig. 4(c) and (f), thermal asymmetry was less pronounced. Similarly situated rods had similar temperatures and exhibited the expected trend toward lower temperatures farther from the center. Moreover, an important thermal spike was present at 1050 and 1150 mm. The thermocouples reporting this spike survived until the end of the test, whereas at the same time in the experiment (i.e., 9000–9100 s), many of the thermocouples at the 850 and 950 mm hot zones failed, potentially because of a similar temperature spike. Both the late-hold thermal spike and thermal asymmetry in the bundle are attributed to thermocouple sheath interactions, as discussed in Sections 3.3 and 3.4.

3.3. Hydrogen release

QUENCH-15 resulted in a bimodal release of H_2, where half of the 47.6 g total H_2 was slowly released during the pre-oxidation stage, the transient resulted in rapid release of 16.6 g of additional H_2, and the final 7.7 g of H_2 was released during the quench stage [18]. QUENCH-19's H_2 release is shown in Fig. 5. The $\log_{10}$ curve of instantaneous hydrogen release rate is shown on the y-axis of Fig. 5 and the cumulative hydrogen release is provided on the second y-axis.

During pre-oxidation, a small amount of H_2, 0.3 g, was produced, as shown in Fig. 5. Initial H_2 release followed by a plateau at 1000 s indicates stable passivation behavior. During the transient, H_2 production increased significantly above pre-oxidation levels. However, by the end of the transient, only 0.1 g of additional H_2 had been produced. During the hold, the H_2 release rate increased linearly from around 0.2 mg/s at the start of the hold to about 5 mg/s by 1600 s into the hold. At the end of the transient, the QUENCH-19 bundle had produced less than 1% of the 47.6 g of H_2 produced during QUENCH-15. The release rate then increased more quickly to about 25 mg/s at the start of the quench, at which point a large spike in H_2 production occurred. Rapid increase in the H_2 production rate has been observed when the Al_2O_3 layer becomes unstable and is no longer protective of the underlying FeCrAl alloy [25,26].

During the hold period, the rate of change of H_2 production increased as the FeCrAl cladding began to fail in the hottest sections of the bundle and in places where thermocouple sheaths reacted with the cladding, as described in Section 3.4. Thus, the combined H_2 production during the hold was 7.4 g. Almost all the remaining 1.4 g of H_2 produced during the quench was produced over an approximately 10 s spike, leading to a total of 9.2 g of H_2 produced throughout the test. This total release is about 20% of the total 47.6 g H_2 release in QUENCH-15, despite the extra 2000s of peak heating. Based on analysis of the thermocouple sheath interactions, approximately 2 g of overall released H_2 was attributed to oxidation of the thermocouple sheaths rather than to the FeCrAl cladding.

3.4. Morphological evaluations

3.4.1. Inspection of corner rods and visual examination of bundle periphery before sectioning

Oxidation was measured on the three withdrawn Kanthal corner rods. Rods B, F, and D were withdrawn at the end of the

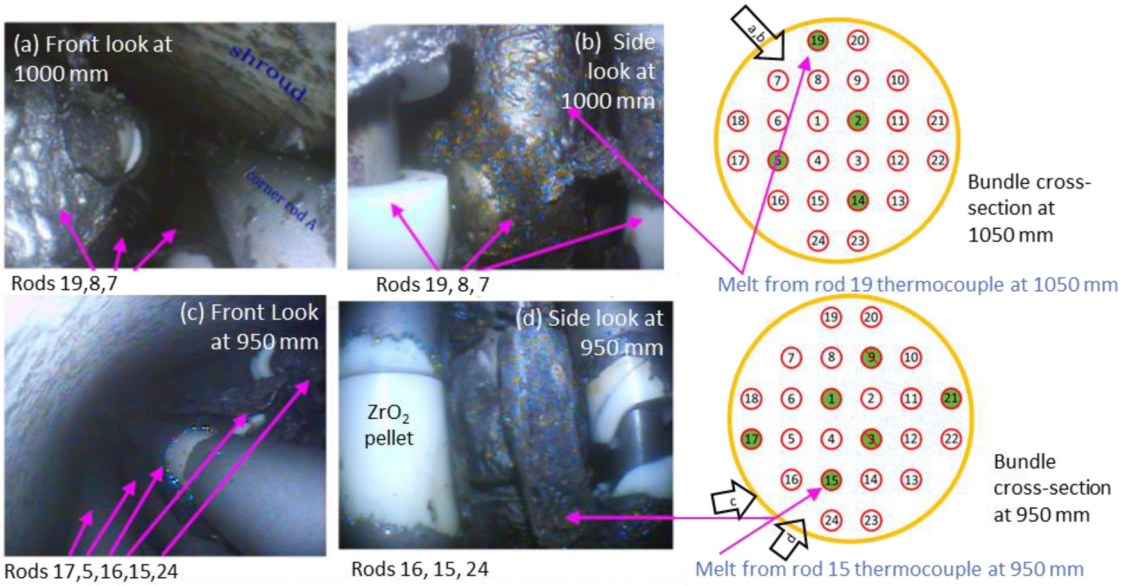

Fig. 6. Videoscope images of the interior of the bundle periphery after the test at (a) and (b) 1000 mm and (c) and (d) 950 mm. A rod numbering diagram at each location from Fig. 1(b) is shown to indicate the position of thermocouple sheaths and rods. White pellets are exposed ZrO_2 pellets.

pre-oxidation, transient, and quench stages, respectively. Each was found to have only slight oxidation of <1 μm. A videoscope, inserted post-test into the bundle on its periphery, showed several features at the 950 and 1000 mm elevations. As shown in Fig. 6, at the examined elevations, significant melt formation was observed that exposed the underlying ZrO_2 pellets and tungsten heater rods. Each of the melt locations correlated with a thermocouple placement. Other images, such as Fig. 6(c), showed cladding gaps, where the cladding is absent but no melt formation, extensive oxidation, or attack of the ZrO_2 pellets is evident. Similar gaps were not observed in the comparator test, QUENCH-15, with Zr-based alloys [2,18]. The higher thermal expansion of FeCrAl compared to Zr-based alloys [27] may have led to fracturing of the rods during the rapid quench process.

AISI 304 steel has a melting temperature between 1400 and 1450°C, which is the temperature range achieved by the highest temperature rods. Melted sheaths attacked the FeCrAl cladding and led to significant oxidation and partial dissolution. The most likely mechanism for such attack is the diffusion of alloying elements of the 304 steel with the FeCrAl alloy. Changing the alloys composition could then lead to alteration of oxidation behavior and melting temperature [28]. The cladding completely melted and oxidized on the inner rods at 950 mm.

3.4.2. *Metallographic examinations of interior rods*

Fig. 7 shows back-scattered electron (BSE) images of the full rod cross sections for rods 3 and 4. Although these rods were nominally exposed to the same conditions because of the symmetry of the system, they showed significantly different microstructures. At 750 mm, rod 4 looked pristine on both sides of the cladding, whereas the cladding of rod 3 was significantly thinned and the cladding–pellet gap was filled with oxidized cladding melt. Interestingly, the inverse was true at 850 mm; rod 3 appeared pristine with no damage to either the ZrO_2 or cladding, whereas damage was present on the interior of the cladding and in one place on the exterior of the cladding of rod 4. At 950 mm, claddings and pellets of both rods were destroyed. Moreover, the damage at 950 mm was so extensive that only small pieces of pellet and cladding were left, and rod 4's pellet had become extremely porous with a fully oxidized cladding nearby.

Figs. 8 and 9 show SEM imaging and EDS spectra of rod 3 cladding and different portions of the rod 3 cladding attack of the ZrO_2. The SEM/EDS analyses in both figures were performed on a metallographic slice at 850 mm that was taken from the other side of the cut in Fig. 7 (i.e., the image was taken from the opposite surface along the cut line). An intact portion of the cladding is shown in Fig. 8, and a heavily oxidized portion is shown in Fig. 9. The intact cladding is revealed to have a thin (i.e., < 3 μm) Al_2O_3 layer, similar to other observed intact cladding throughout the bundle. Fig. 9 shows an area of the same rod section from which Fig. 8 was taken, but Fig. 9 shows only heavily oxidized cladding that had fused to the underlying ZrO_2 pellet.

As shown in Fig. 9, the bulk of the cladding remnant was mixed oxide. In some areas, such as the interface imaged in Fig. 9, the cladding was composed of metallic iron. In most areas examined, the cladding remnant looked similar to Fig. 9(c), where precipitates of Cr and Al oxides were distributed into the matrix of the frozen FeO melt, which formed at temperatures above 1380°C. Where not pristine, the ZrO_2 pellets contained a significant amount of FeO interspersed among ZrO_2 crystallites with a large amount of porosity, see Fig. 9(a). It is not clear whether porosity was caused by metallographic processing or test conditions. Although the latter seems more likely given the metallographic features observed within the ZrO_2, some grain clusters were observed to fall out during grinding and polishing. On the internal portion of the cladding, some areas were heavily damaged between the residual metal cladding and pellet, as shown at low magnification in Fig. 7 on rod 3 at 750 mm. One such area is shown in Fig. 10 for a middle rod, rod 16, at 850 mm. Fig. 10(a) shows an SE image of internal cladding attack. The unreacted portion of the cladding is shown at the bottom of Fig. 10(a). Above the cladding is a complex oxide mixture containing FeO, Cr_2O_3, and Al_2O_3. Fig. 10(b) shows an O K_α map of the same region, and metallic oxides are revealed in Fig. 10(c), which shows a layered EDS map of Fe, Cr, and Al. The ZrO_2 pellet is above the complex oxide mixture, out of the image frame. The interior, damaged rod cladding and pellet showed similar microstructure wherever the damaged cladding appeared.

Fig. 11 shows the beginning phase of damage to ZrO_2 pellets; SE imaging is shown in addition to BSE imaging for three of the internal rods at 750 mm. For all rods examined, damage that occurred during the beginning phase consisted of heavy oxidation of

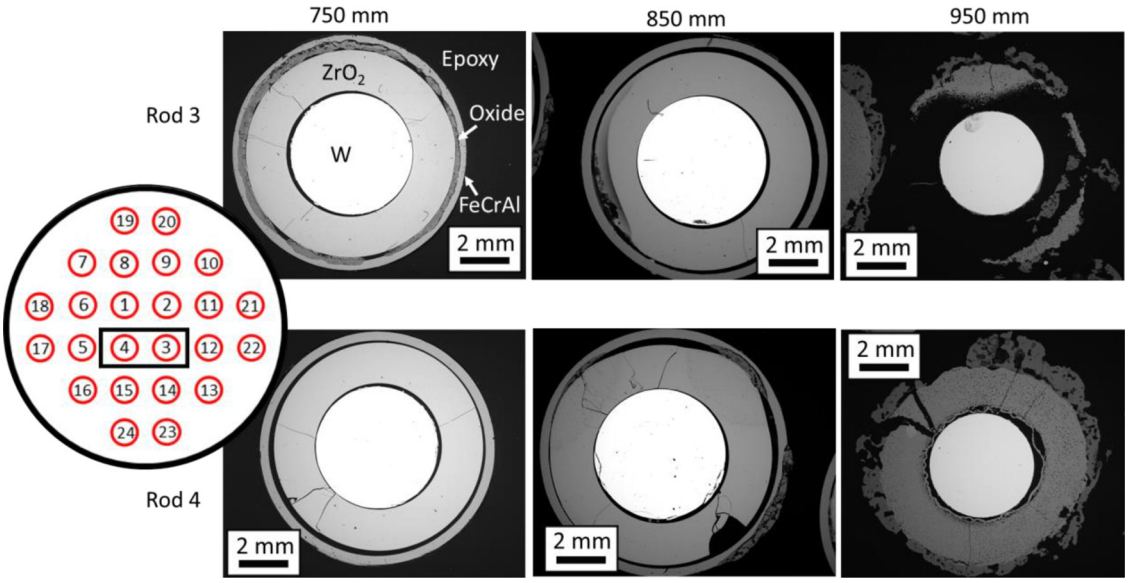

Fig. 7. Low-magnification BSE images of rods 3 (top row) and 4 (bottom row) at 750, 850, and 950 mm (columns 1-3, respectively). A rod diagram to the left shows the locations of rods 3 and 4 within the bundle with a black box.

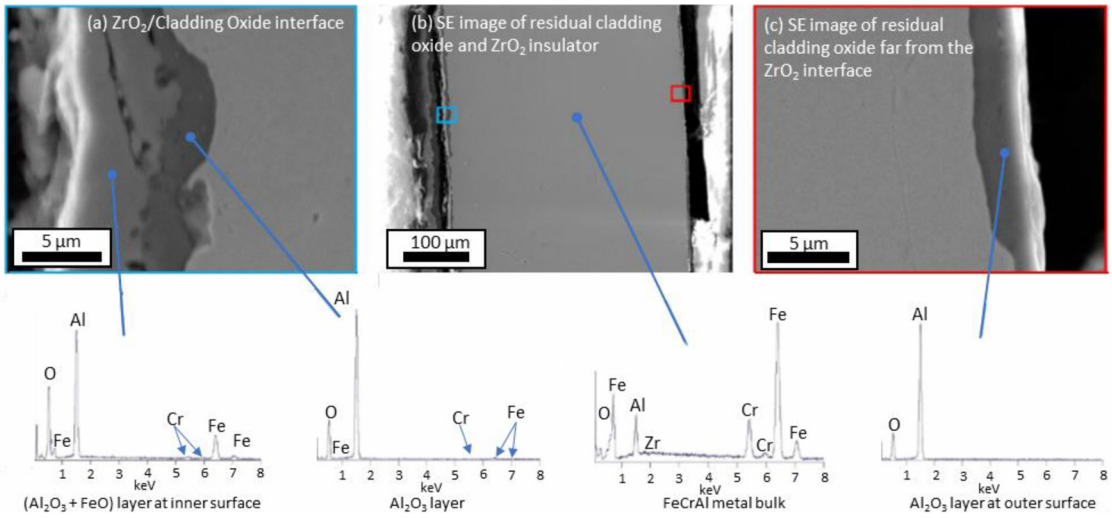

Fig. 8. SEM/EDS analysis of an intact (unreacted) portion of the rod 3 cladding at ~855 mm. A lower magnification image of the entire cladding (b) shows two colored boxes corresponding to (a) and (c) on the left and right of (b), respectively. The blue (a) and red (c) boxes show inner and outer cladding edges, respectively, revealing a protective alumina layer on the exterior, as well as a partially attacked alumina layer on the interior where cladding melt relocation had mixed with the alumina layer.

the cladding interior, caused by direct melting and oxidation of the cladding or by the effects of melt flows from higher elevations interacting with pellets at lower elevations. SE imaging revealed locations of damage on ZrO_2 pellets, as a contrast, change because of reduced charging where Fe was incorporated into the ZrO_2. On rod 1 at 750 mm, shown in Fig. 11(a) and (b), about three-quarters of the pellets showed signs of attack consistent with a similar amount of internal damage to the cladding. However, not all internal rods showed internal attack. Rod 3, shown in Fig. 11(c) and (d), showed more extensive internal attack and cladding thinning than rod 1, whereas rod 4, shown in Fig. 11(e) and (f), appeared pristine. Interestingly, a thermocouple sheath was present at the top left of rod 1 (called out in Fig. 11b), but no external attack of the cladding was identified, implying that the temperature at 750 mm did not reach the failure temperature of the thermocouples.

At 850 mm, as shown in Figs. 7 and 12, the damage was more heterogeneous. Rods 1, 3, and 4 showed little or no damage. However, rod 2, shown in Fig. 12(c) and (d), lost its pellet and cladding. Only a small portion of the pellet and the remnant of oxidized cladding was identified, and the resulting fused piece was displaced from the tungsten element. As shown in Fig. 1(b), a thermocouple was welded at 850 mm. This thermocouple failed about 100 s before the quench step and reached the reported bundle maximum temperature of 1455°C before failure.

Finally, at the highest elevation examined, 950 mm, the cladding was partially to heavily relocated, and the pellet was made weak, porous, and in some cases fully destroyed. The two internal rods not shown here (rods 3 and 4) had similar morphology to Fig. 7. This was the case independent of the placement of thermocouples, which were present on rods 1 and 3.

3.4.3. Metallographic examination of midrange and exterior rods

Middle rods (5–16) and exterior rods (17–24) showed morphological features similar to those of the interior rods at each elevation, although in general less damage occurred farther from the center. Most rods were at least partially intact, and a thin oxide on intact cladding was observed, implying adequate protection of the cladding in these regions. On defected and destroyed regions,

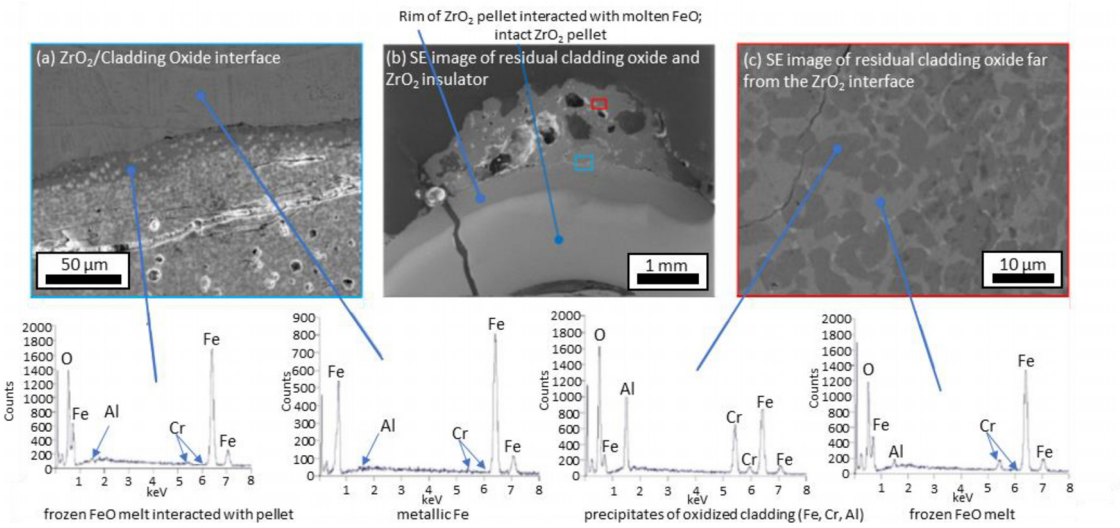

Fig. 9. SEM/EDS analysis of rod 3 at 850 mm elevation showing interaction of molten oxide melt with pellet. (b) shows a low-magnification secondary electron (SE) image of the fully oxidized cladding fused to the underlying ZrO_2 pellet. (a), which corresponds to the blue box in (b), shows a higher-magnification image of the interface between the pellet and cladding oxides. (c), which corresponds to the red box in (b), is a high-magnification image of the bulk cladding oxide. Four EDS spectra are also presented, showing the elemental compositions of primary constituent regions.

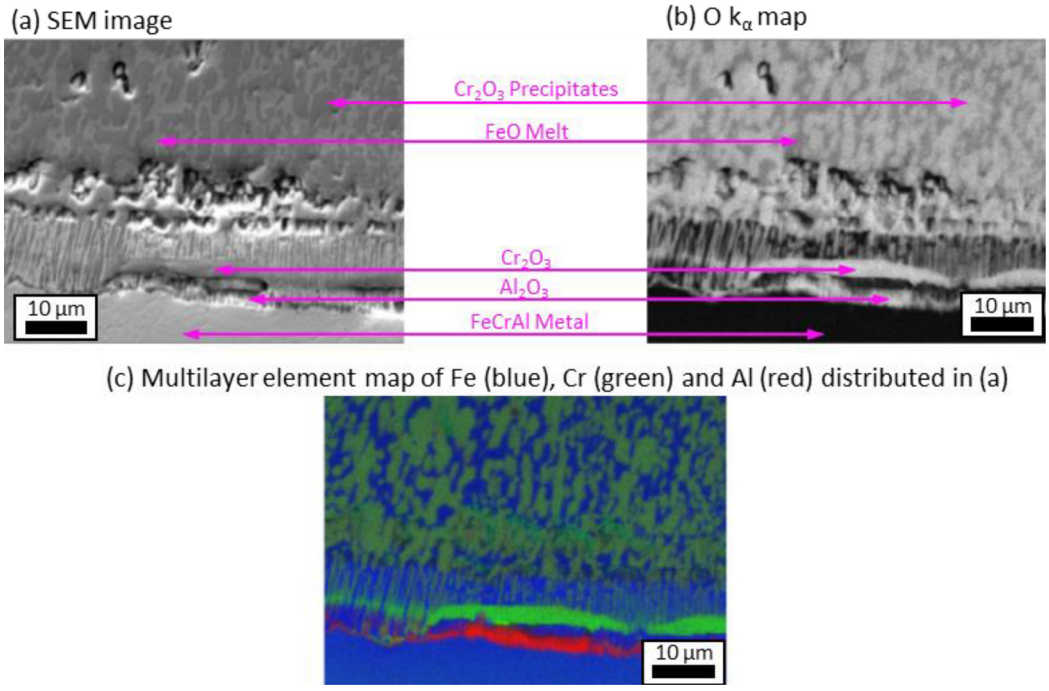

Fig. 10. Localized internal oxidation of rod 16 at 850 mm. Cr_2O_3, FeO, and Al_2O_3 oxides were all identified in distinct phases and dendrites at different regions from the cladding surface.

remnant cladding and pellets were similar to the oxides shown in Fig. 9.

As with the internal rods, middle and external rods at 750 mm were found to be intact (see Figs. 13–15) with only a few isolated instances of significant oxidation, such as in rod 14 shown in Fig. 14. As shown in Fig. 1(b), rods 6 and 8 were placed next to rod 1, where a thermocouple was initially welded. As with internal rod 1, the presence of a thermocouple sheath near rods 6 and 8 appeared not to affect their cladding.

However, at 850 mm, significant chemical attack of the rods was evident. Fig. 13 shows the impact of thermocouple location on chemical attack. Whereas interior rod 2 was fully destroyed where attached to a thermocouple, at the mid-range rod 8 (and for the similarly placed exterior rod 19, shown in Fig. 17) the presence of a thermocouple sheath adjacent to the rod led to attack and failure of the rod local only to the location of the thermocouple.

The same rods 6 and 8 at 950 mm were also affected by thermocouple placement. Rod 6, shown in Fig. 13, did not contact the thermocouple at rod 1. Regardless, about one-third of the cladding in the direction of the thermocouple was destroyed, and the other portion was left intact. Importantly, the bottom right of that cladding, facing inward toward the center of the core, was left intact. Rod 8 was similarly damaged.

Rods 14 and 16, shown in Fig. 14, showed less damage related to thermocouple placement, in contrast to rods 6 and 8; both 14 and 16 were pristine and 750 mm and 850 mm. At 950 mm with

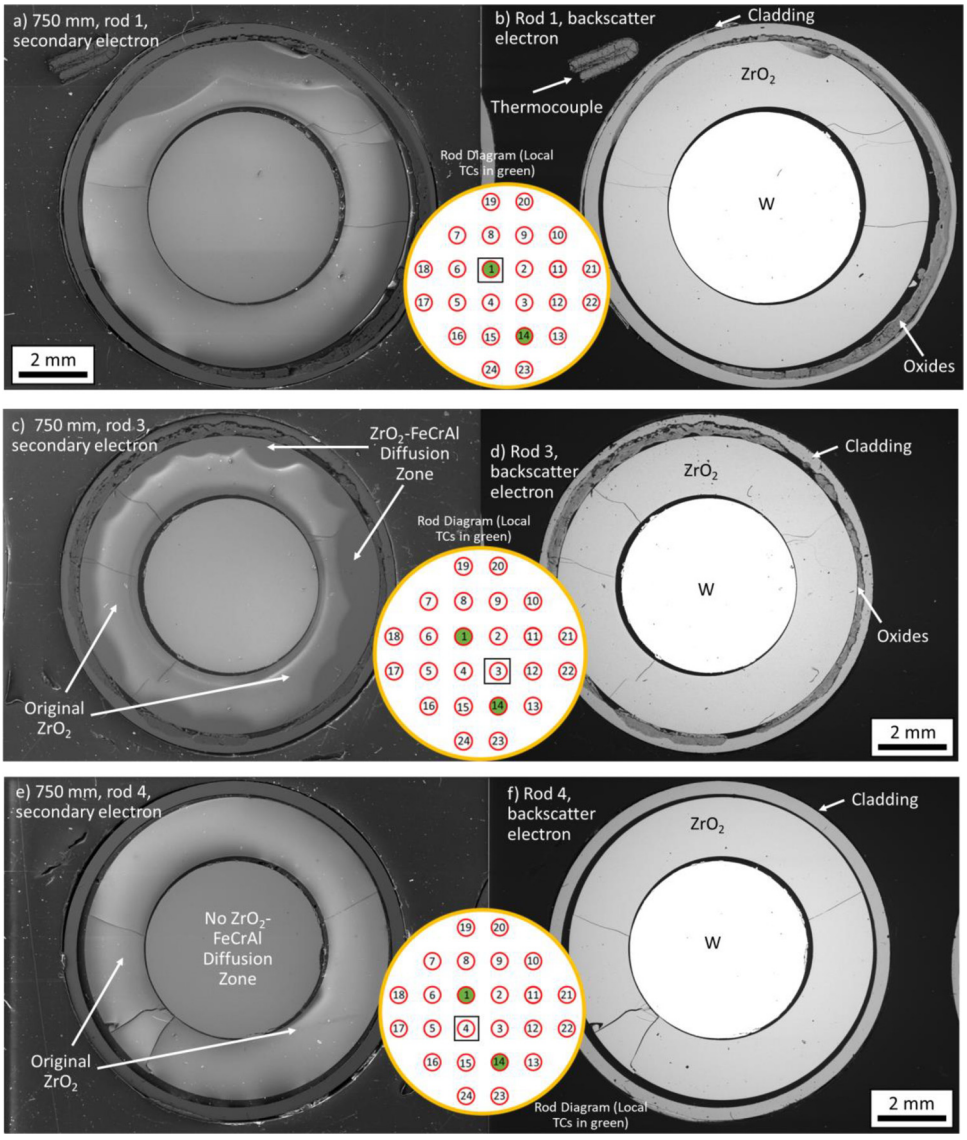

Fig. 11. Low-magnification SE (a, c, e) and BSE (b, d, f) images of rods 1, 3, and 4 at 750 mm.

2 thermocouple sheaths in proximity to rod 16, no damage was evident on rod 16. However, on rod 14 the entire rod was heavily damaged at 950 mm. As noted in Fig. 2(b), at 950 mm, the interior rod 3 thermocouple, which failed prior to the test, was in proximity to rod 14 and the higher temperature of the interior rods may have led to the additional damage on rod 14. In contrast, the middle and exterior rod thermocouples surrounding rod 16 were sufficiently cool to prevent thermocouple attack on rod 16.

Again, a thermocouple sheath was present running up to 850 mm at rod 22, yet no damage was observed, implying that thermocouple-related attack temperatures were not reached at 750 mm. Damage was observed, however, with increasing elevation. At 850 mm, shown in Fig. 16, the presence of thermocouple sheaths strongly correlated to attack on rods 21, 19, and 22. However, rod 17, where no thermocouple was placed, was left pristine, and damage on rods 19 and 21 was limited to the locations of the thermocouples and nearby cladding region. However, rod 22's cladding fully disappeared, but with only a small portion of the underlying ZrO_2 exhibiting damage on the top right. It is possible that rapid quenching of the bundle led to local failure of the rod due to a high coefficient of thermal expansion [27], rather than oxidation or melt-formation attack. At 950 mm, shown in Fig. 17, the morphology was similar to the morphology at 850 mm. Rod 17 was missing the cladding but no evidence of ZrO_2 attack was seen, implying rapid mechanical failure of the cladding in that position. Within the mount itself, some cladding was visually observed, although it did not protrude from the surface of the epoxy. Rods 19 and 21 showed extensive attack. Rod 19 did not have a thermocouple next to it, but it is possible that heating from the melt and subsequent oxidation of the thermocouple sheath going down to 950 mm led to attack on rod 19. The mixed oxide debris on rod 19 is focused in the direction of the rod 8 thermocouple. On rod 21, the entire cladding was missing, and three-quarters of the ZrO_2 pellet was damaged, with some cladding remnant oxide fused to it. Rod 21 was originally connected to a thermocouple, which failed near the end of the hold portion of the test.

4. Discussion

Of the various differences between this test and QUENCH-15, two are most relevant to the results of this test. First, prior to the test and through much of the pre-oxidation stage, the shroud annulus was at least partially filled with water. Second, the thermo-

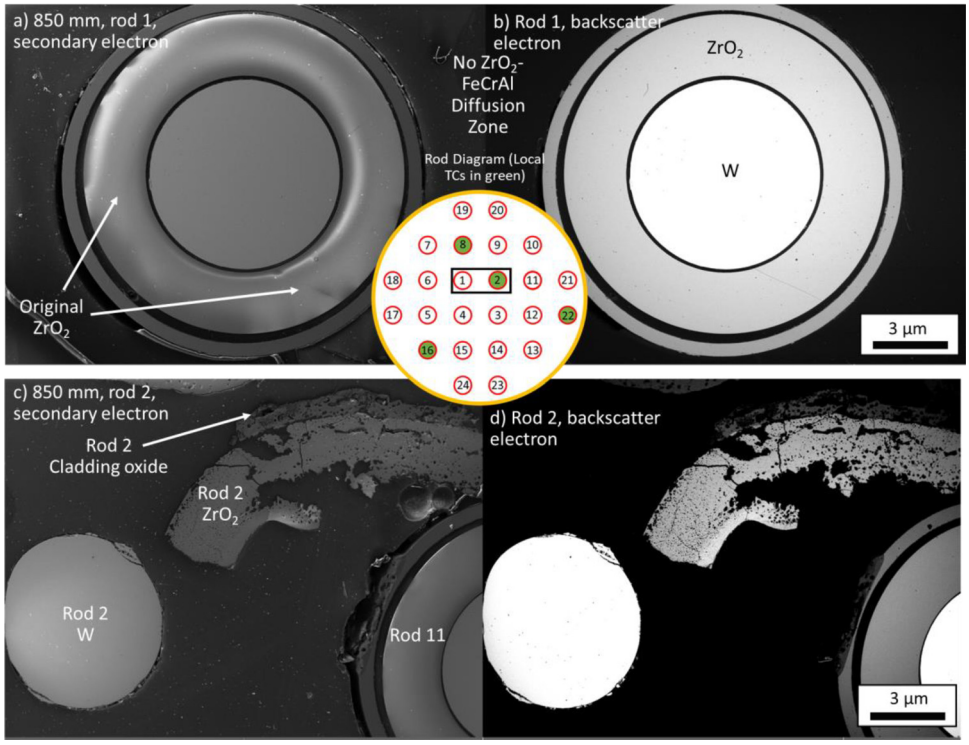

Fig. 12. Low magnification SE and BSE images of rods 1 (a, b), and2 (c, d) at 850 mm. In (c) and (d), the rod was fully destroyed.

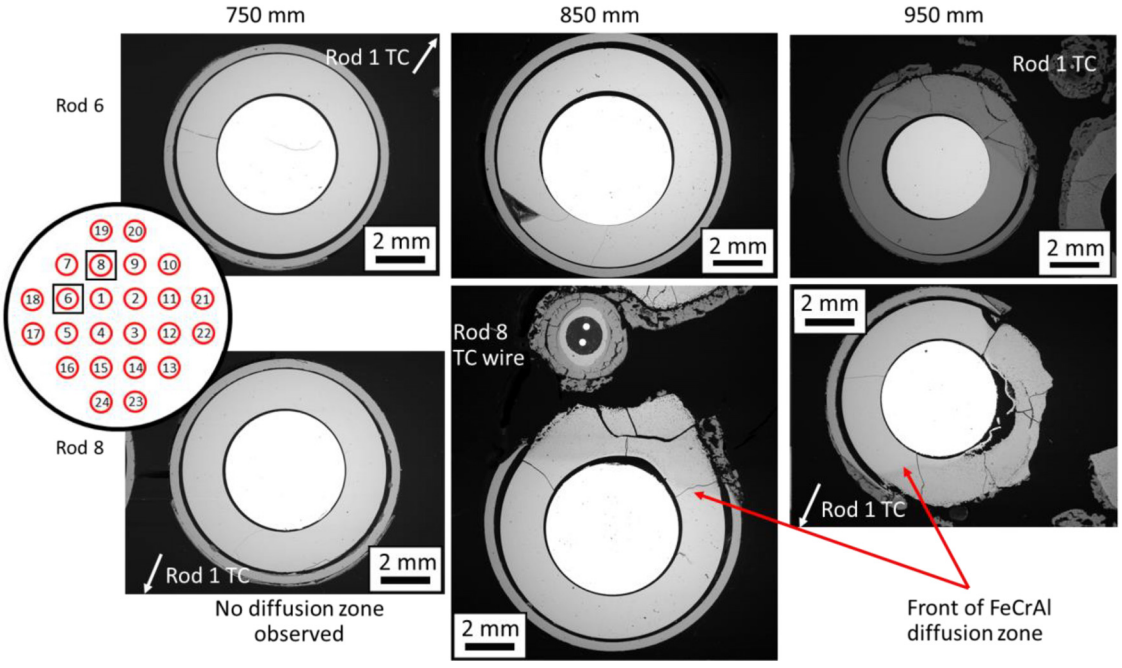

Fig. 13. Low-magnification BSE images of rods 6 (top row) and 8 (bottom row) at 750, 850, and 950 mm (columns 1-3, respectively). A rod diagram is shown on the left of the figure with a black box around rods 6 and 8.

couple sheath materials interacted significantly with the cladding materials at the hottest locations.

The first of these was a major divergence from the QUENCH-15 boundary condition. By reducing the shroud wall temperature, this divergence from planned behavior had the potential to impact the test by reducing the heating during pre-oxidation, thereby reducing the overall temperature of the rods during the transient and hold portions of the test. However, this concern can be dismissed by considering the H_2 release rate and temperature profiles during pre-oxidation, shown in Fig. 5 and Fig. 3, respectively. Compared to QUENCH-15, the pre-oxidation curve for QUENCH-19 is approximately 200°C cooler both as the rods were heating up and at the onset of the transient. In QUENCH-15, after the initial pre-oxidation was complete, the maximum temperature profile reached a near-steady value and even decreased slightly until the onset of the transient. Despite the delayed heating of the shroud wall due to water retention in QUENCH-19, similar thermal behavior was seen at the 850 mm elevation. Whereas initial heating was slower than

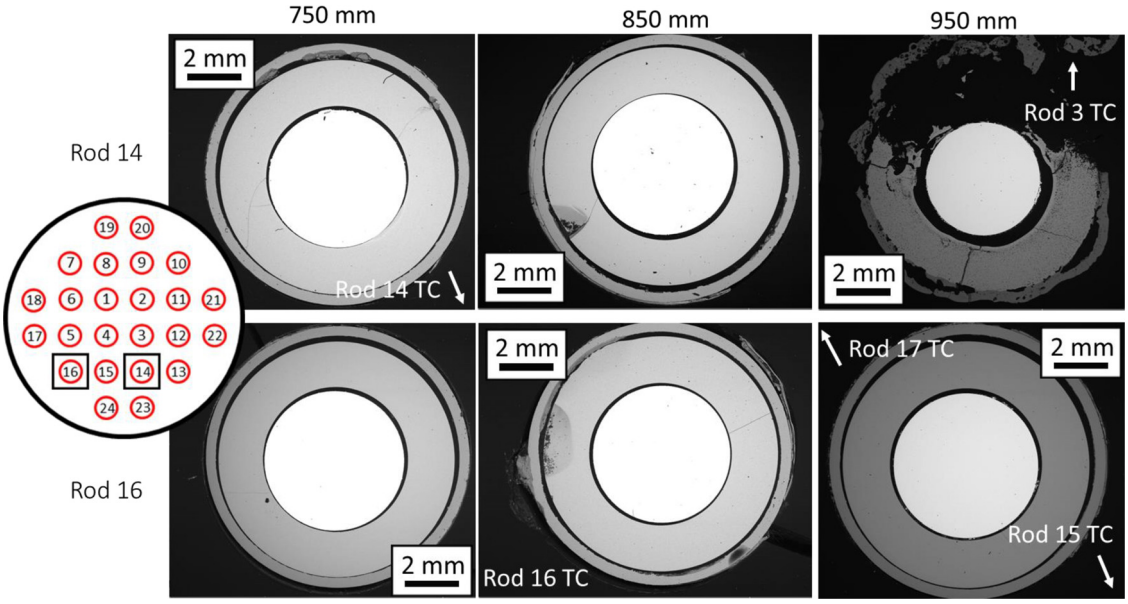

Fig. 14. BSE images of rods 14 (top row) and 16 (bottom row) at 750, 850, and 950 mm (columns 1-3, respectively). External rod morphology is shown in Fig. 15–Fig. 17. At 750 mm, these external rods were found to contain metal shavings (for example, Fig. 15(d) at the top of the image between the cladding and ZrO_2, where no damage is observable, but metal shavings are present) but were otherwise pristine. Shavings were found to be unoxidized and were attributed to the cutting and polishing process, rather than a feature of the experiment. After polishing, the epoxy was observed to have partially cracked in some areas and separated from the edges of some of the cladding, providing some space for shavings to have deposited during the grinding/polishing process.

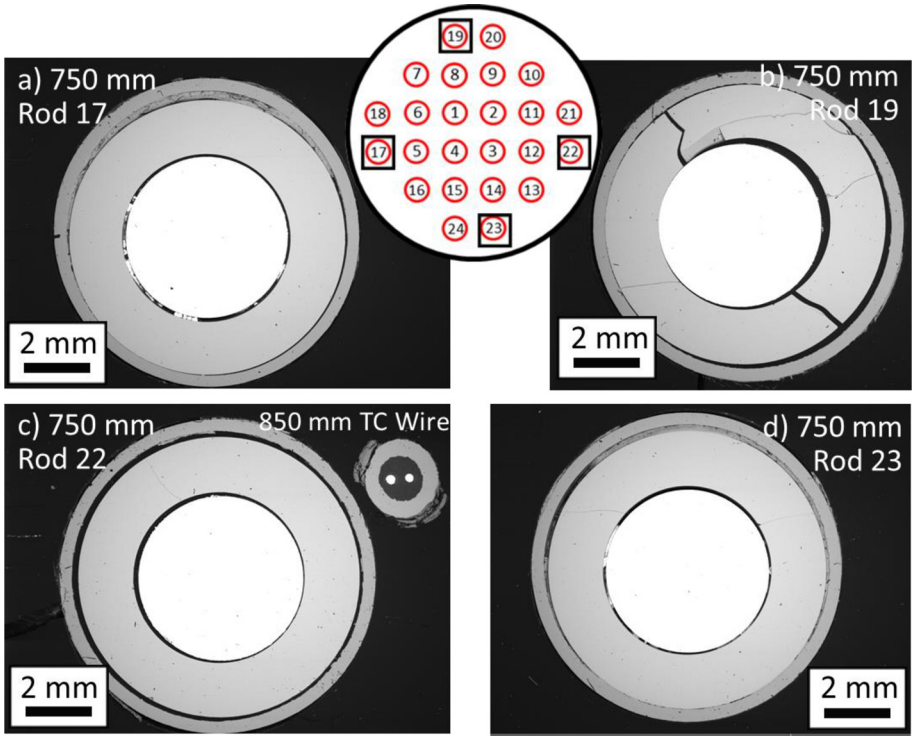

Fig. 15. BSE images of the external rods 17, 19, 22, and 23 at 750 mm. Black boxes in the rod diagram at the top of the figure show the locations of the rods.

in QUENCH-15 and the shroud at 850 mm did not increase in temperature until over 2000 s, the power profile in QUENCH-19 closely approximated the temperature profile for approximately 1500 s of the 6,000 s pre-oxidation, as shown in Fig. 3. In addition, the instantaneous H_2 release rate, shown in Fig. 5, increased until around 3500 s and then declined to a steady level through the rest of the pre-oxidation, similarly to the instantaneous H_2 release rate in QUENCH-15 [18]. Both of these features are similar in kind to pre-oxidation behavior in QUENCH-15 and indicate the formation of a stable oxide film and heat transfer equilibrium.

Secondly, in addition to electrical power through the tungsten heaters, the rod temperature is also a function of the heat released during formation of the oxides during pre-oxidation, which will be carried off in the hydrogen gas and deposited on the cladding tube walls. By analyzing the amount of H_2 released during pre-oxidation of QUENCH-15, it is estimated that pre-oxidation produced about 3.5 MJ. However, this is only just over 5% of the pre-oxidation electrical input energy. Naturally, oxidation-induced heating is localized, rather than spread uniformly over the entire rod length the way electrical heating is fairly uniform. However, during the pre-

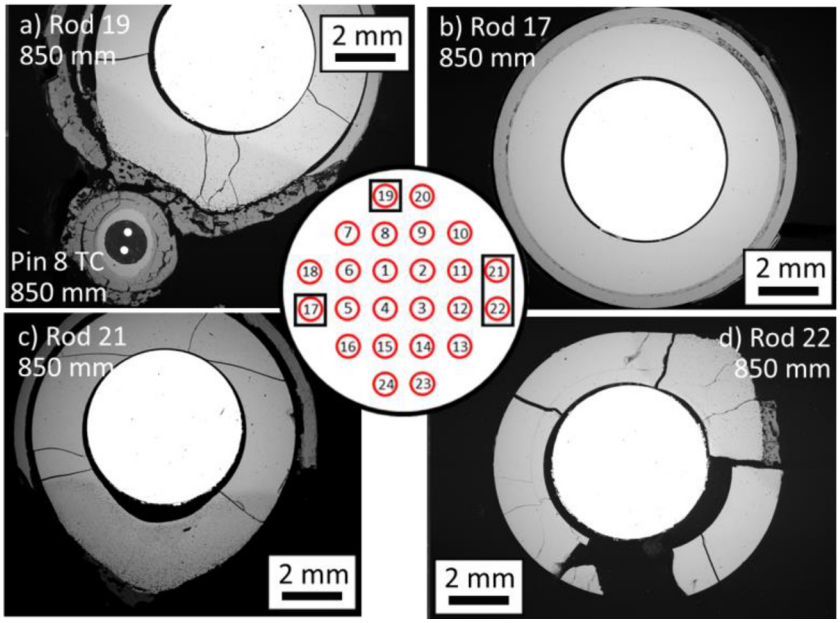

Fig. 16. BSE images of the external rods 19, 17, 21, and 22 at 850 mm. Black boxes in the rod diagram at the top of the figure show the locations of the rods.

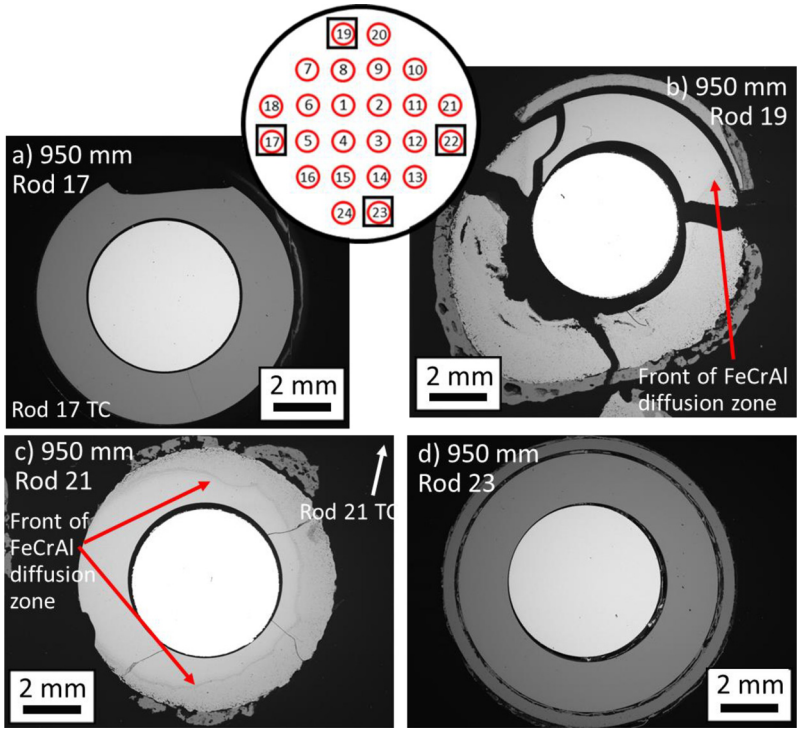

Fig. 17. BSE images of the external rods 17, 19, 21, and 23 at 950 mm. Black boxes in the rod diagram at the top of the figure show the locations of the rods.

oxidation stage the oxidation was well distributed over the heated length of the rod [18], reducing the likelihood of significant localized heat buildup. As a result, the temperature differential between QUENCH-15 and QUENCH-19 at the beginning of the transient was likely related to the material system itself, in particular to the much thicker (i.e., up to a few hundred micrometers) oxide that formed on ZIRLO during the QUENCH-15 test, rather than the pre-oxidation boundary condition.

The second test divergence relates to the thermocouple sheath materials, which played a critical role in the test behavior. Failure of the sheath and associated thermocouples in the hottest regions of the bundle prevented additional temperature collection at those points. If further increases in temperature occurred after thermocouple failure, those temperature transients were not recorded. Although similar sheath melting occurred at the end of the QUENCH-15 test, the ZIRLO cladding and sheath material had dissimilar melting temperatures and no interaction was observed between them. This was due, in part, to the few-hundred-micrometer-thick oxide separating the ZIRLO and sheath materials. By contrast, in QUENCH-19 all thermocouples were welded to the cladding walls,

eliminating any oxidation barrier to interaction. In the hottest elevations of the test, 850 and 950 mm, thermocouple sheaths reacted aggressively with the FeCrAl cladding, leading to extensive melt formation and subsequent oxidation, as well as to degradation of the ZrO_2 pellets. This behavior is similar to previously observed attack of UO_2 by FeO [29]. Additionally, some of this melt flowed down to lower elevations, causing thinning of the cladding wall.

This type of sheath-cladding melt and oxidation behavior was implicated in almost all the oxidation damage in the QUENCH-19 test, most notably for the 850 mm internal rods and the middle and external rods at 950 mm, where location relative to thermocouples was the determining factor in cladding failure. However, thermocouples were not exclusively implicated in rod degradation in the bundle center at 950 mm. Two thermocouples were initially placed centrally at 950 mm, but all four rods were also heavily oxidized. In addition to the rods in direct contact with thermocouple sheaths (rods 1 and 3), rod 2 was connected to a thermocouple at 850 mm, and there may have been enough energy generated by the sheath–cladding interactions and oxidation to facilitate damage at the 950 mm elevation. Rapid high-temperature oxidation has previously been reported for FeCrAl alloys [23, 25]. If rod 4 was not affected by the melt-oxidation behavior around it, then the full destruction of the rod 4 cladding (see Fig. 7) may have been due exclusively to a higher-than-recorded temperature occurring in the bundle center. In this event, the temperature likely exceeded 1500°C at 950 mm in the bundle center. It is not clear whether such a temperature spike would have occurred without the heating from the sheath-cladding melt and oxidation process. However, the clear thermal asymmetry in the bundle in addition to the significant amount of estimated H_2 produced by the thermocouple sheath melting and oxidation (~20% of the total QUENCH-19 amount) suggests that the adverse thermocouple behavior may have added significant heat.

Additionally, H_2 release was found to be minimal. For the entirety of the test, only 9.2 g of H_2 was produced: 0.3 g during pre-oxidation, 0.1 g during the transient, 7.4 g during the hold period, and 1.4 g during quench. This release is only about 20% of the total release during QUENCH-15, which totaled 47.6 g H_2: 23.3 g during pre-oxidation, 16.6 g during the transient, 7.7 g during quench. These numbers are clearly reflected in very thin oxides in QUENCH-19, excepting regions highly damaged by the thermocouple sheath-cladding reactions. As shown in Fig. 5, H_2 release took a few hundred seconds to increase once the transient started. The release rate steadily increased until it began to increase more rapidly at about 8000 s and about 8740 s. These increases are likely the result of two phenomena. First, above 1300°C the Al_2O_3 layer is mechanically destabilized, allowing greater steam access to the surface and thus faster corrosion as the oxide layer is rebuilt and eventually spalls [26]. Because the entire bundle does not reach 1300°C at the same time, around 7,800 s the H_2 generation rate increased and finally transitioned to the second regime by about 8200 s. The second regime occurred more abruptly and likely corresponded to the onset of thermocouple sheath and cladding interactions. Because of thermal variations in the bundle, not all thermocouples that failed did so immediately, but the first failure at 950 mm on rod 1 coincided almost exactly with the second increase in the H_2 generation rate. It is possible that this second transition region would have occurred without the influence of thermocouples [23, 25, 26]. However, its impact would have been reduced because the FeCrAl would have been deprived of a secondary heat source: the heat of oxidation of the thermocouple sheath materials and sheath-cladding melt mixtures. Together with the higher melting point of B136Y3, the H_2 production would have been limited. If this second increase in gas rate had not occurred, then an additional few grams of H_2 release would have been avoided.

Nevertheless, it cannot be completely ruled out that an iron (II) oxide melt, FeO, formed without the influence of thermocouples. It may have formed because of the interaction of steam with the outer cladding surface after the destruction of the alumina layer [30]. The other explanation could be the observed mechanically induced cracking and loss of the cladding material (for example in Fig. 7a), which allow steam to penetrate into the gaps between the pellet and the cladding at high temperatures. This can cause intense high-temperature oxidation of the inner cladding surface, which is not protected by a preformed alumina layer, causing the formation of a FeO melt at temperatures above 1380°C for pure FeO. Additionally, as previously reported by Bechta et al. [31], the ZrO_2-FeO system forms a 1330°C eutectic at around 13% FeO in ZrO_2. After initial internal FeO formation, the attack of the ZrO_2 may have led to formation of lower temperature melts and allowed ZrO_2-FeO mixtures to penetrate further down the test bundle before fully solidifying. This is an important point due to the destructive effect of such a melt on the integrity of the pellet material and should be investigated further.

5. Conclusion

The QUENCH-19 test was conducted with conditions similar to those in QUENCH-15. Primary differences between QUENCH-15 (which tested Zr-based cladding) and QUENCH-19 were (1) the material system tested was B136Y3, (2) the addition of a 2000 s hold period because of the accident tolerance of the cladding, (3) a slightly lower temperature inlet gas temperature (i.e., 20–50°C lower, depending on the progression time of the test), and (4) significant shroud insulation wetting at the start of and through some of the pre-oxidation heating. The first two differences were intentional, with the goal of understanding the limits of FeCrAl-class B136Y3 alloys undergoing an accident condition. The latter two were experimental artifacts but were determined unlikely to have significant adverse effects on the test.

No breakaway oxidation was observed during the test, and oxide thicknesses away from damaged areas were uniformly only a few micrometers. However, several of the thermocouples were found to have failed due to melting of the thermocouple sheaths and cladding followed by complete oxidation of the melt. This melt caused significant local rod damage by thinning the cladding wall where the melt (mostly FeO) traveled, partially destroying the pellets, and causing excess H_2 release. The maximum actual temperature is not known due to the thermocouple failure. The maximum temperature observed was 1455°C, but the temperature may have reached over 1500°C, as can be inferred by apparent cladding failure without obvious thermocouple effects. A significant part of observed melt mixtures was related to thermocouple damage: only portions of cladding contacting or near thermocouple sheaths were affected. Finally, in select areas, the cladding appeared to have broken rather than melted. These areas were observed visually and in the metallographic mounts and may have occurred due to the high thermal expansion of FeCrAl.

Despite these artifacts, from this test B136Y3 FeCrAl alloys in reactor can be expected to have improved survivability compared to Zr-based alloys in a LOCA. In addition to a largely protective oxide on most of the cladding, even with the longer hold period, the hydrogen generation was substantially less than in the similar QUENCH-15 test with Zr-based alloys. However, additional work should be performed to understand the likelihood of localized melting, and the effect of CTE on local fracture of the cladding during quenching.

Declaration of Competing Interest

The authors declare that they have no known competing financial interests or personal relationships that could have appeared to influence the work reported in this paper.

CRediT authorship contribution statement

Peter Doyle: Investigation, Writing – original draft, Writing – review & editing, Visualization. **Juri Stuckert:** Methodology, Investigation, Writing – review & editing, Visualization. **Mirco Grosse:** Methodology, Investigation, Writing – review & editing, Visualization. **Martin Steinbrück:** Methodology, Investigation, Writing – review & editing, Visualization. **Andrew T. Nelson:** Supervision, Writing – review & editing. **Jason Harp:** Supervision, Writing – review & editing. **Kurt Terrani:** Conceptualization, Funding acquisition, Writing – review & editing.

Data Availability

Data will be made available on request.

Acknowledgments

The authors would like to acknowledge the staff at KIT—particularly J. Moch and U. Peters for bundle preparation and U. Stegmaier for SEM/EDS investigations—for their excellent work in running this experiment and providing extensive data sets and preparation of metallographic mounts. We further thank Emma Shamblin for helpful technical edits and Matt Kurley and Mackenzie Ridley for their technical reviews. The work was supported by the Advanced Fuels Campaign of the United States Department of Energy Office of Nuclear Energy.

References

[1] L.J. Ott, K.R. Robb, Simulation of QUENCH-15 and preliminary pre-test predictions for QUENCH-19, Oak Ridge National Laboratory, 2018. This is technical report and can be accessed in full at https://www.osti.gov/biblio/1459285.

[2] M. Steinbrück, M. Große, L. Sepold, J. Stuckert, Synopsis and outcome of the QUENCH experimental program, Nuclear Eng. Des. 240 (2010) 1714–1727, doi:10.1016/j.nucengdes.2010.03.021.

[3] J. Stuckert, M. Grosse, M. Steinbrück, K. Terrani, Results of the bundle test QUENCH-19 with FeCrAl claddings, in: Proceedings of the Global/Top Fuel, Seattle, WA, American Nuclear Society, Seattle, WA, USA, 2019, pp. 922–927. September 22-26.

[4] K.R. Robb, M. Howell, L.J. Ott, Parametric and Experimentally Informed BWR Severe Accident Analysis Utilizing FeCrAl - (M3FT-17OR020205041), U.S. Department of Energy, Oak Ridge, 2017 https://www.osti.gov/servlets/purl/1399971.

[5] K.R. Robb, J.W. Mcmurray, K.A. Terrani, Severe Accident Analysis of BWR Core Fueled with UO_2/FeCrAl with Updated Materials and Melt Properties from Experiments, 2016.

[6] T. Haste, M. Steinbrück, M. Barrachin, O. De Luze, M. Grosse, J. Stuckert, A comparison of core degradation phenomena in the CORA, QUENCH, Phébus SFD and Phébus FP experiments, Nuclear Eng. Des. 283 (2015) 8–20, doi:10.1016/j.nucengdes.2014.06.035.

[7] J. Stuckert, M. Grosse, M. Steinbrück, M. Walter, A. Wensauer, Results of the QUENCH-LOCA experimental program at KIT, J. Nuclear Mater. 534 (2020) 152143, doi:10.1016/j.jnucmat.2020.152143.

[8] J. Stuckert, M. Steinbrück, M. Grosse, Experimental program QUENCH at KIT on core degradation during reflooding under LOCA conditions and in the early phase of a severe accident, in: Proceedings of the Modelling of Water Cooled Fuel Including Design Basis and Severe Accidents", IAEA, 2015, pp. 281–297. Chengdu, China, 28 October–1 November 2013.

[9] B.A. Pint, K.A. Terrani, Y. Yamamoto, L.L. Snead, Material selection for accident tolerant fuel cladding, Metall. Mater. Trans. E 2 (2015) 190–196, doi:10.1007/s40553-015-0056-7.

[10] B.A. Pint, K.A. Terrani, M.P. Brady, T. Cheng, J.R. Keiser, High temperature oxidation of fuel cladding candidate materials in steam–hydrogen environments, J. Nuclear Mater. 440 (2013) 420–427, doi:10.1016/j.jnucmat.2013.05.047.

[11] K.A. Gamble, T. Barani, D. Pizzocri, J.D. Hales, K.A. Terrani, G. Pastore, An investigation of FeCrAl cladding behavior under normal operating and loss of coolant conditions, J. Nuclear Mater. 491 (2017) 55–66, doi:10.1016/j.jnucmat.2017.04.039.

[12] C.P. Massey, K.A. Terrani, S.N. Dryepondt, B.A. Pint, Cladding burst behavior of Fe-based alloys under LOCA, J. Nuclear Mater. 470 (2016) 128–138, doi:10.1016/j.jnucmat.2015.12.018.

[13] B.A. Pint, S. Dryepondt, K.A. Unocic, D.T. Hoelzer, Development of ODS Fe-CrAl for compatibility in fusion and fission energy applications, JOM 66 (2014) 2458–2466, doi:10.1007/s11837-014-1200-z.

[14] K.A. Terrani, Accident tolerant fuel cladding development: Promise, status, and challenges, J. Nuclear Mater. 501 (2018) 13–30, doi:10.1016/j.jnucmat.2017.12.043.

[15] M. Steinbrück, U. Stegmaier, M. Große, L. Czerniak, E. Lahoda, R. Daum, K. Yueh, High-temperature oxidation and quenching of chromium-coated zirconium alloy ATF cladding tubes with and w/o pre-damage, J. Nuclear Mater. 559 (2022) 153470, doi:10.1016/j.jnucmat.2021.153470.

[16] M. Steinbrück, M. Grosse, U. Stegmaier, J. Braun, C. Lorrette, Oxidation of silicon carbide composites for cuclear applications at very high temperatures in steam, Coatings 12 (2022), doi:10.3390/coatings12070875.

[17] C. Tang, M. Stueber, H.J. Seifert, M. Steinbrück, Protective coatings on zirconium-based alloys as accident-tolerant fuel (ATF) claddings, 35 (2017) 141–165. doi:10.1515/corrrev-2017-0010.

[18] J. Stuckert, M. Große, U. Stegmaier, M. Steinbrück, Results of severe fuel damage experiment QUENCH-15 with ZIRLO cladding tubes. KIT Scientific Reports; 7576, Karlsruher, 2011. doi:10.5445/KSP/1000022788.

[19] J. Stuckert, J. Birchley, M. Große, T. Haste, L. Sepold, M. Steinbrück, Experimental and post-test calculation results of the integral reflood test QUENCH-12 with a VVER-type bundle, Ann. Nucl. Energy 36 (2009) 183–192, doi:10.1016/j.anucene.2008.11.024.

[20] S.S. Raiman, K.G. Field, R.B. Rebak, Y. Yamamoto, K.A. Terrani, Hydrothermal corrosion of 2nd generation FeCrAl alloys for accident tolerant fuel cladding, J. Nuclear Mater. 536 (2020) 152221, doi:10.1016/j.jnucmat.2020.152221.

[21] Z. Liu, Y. Li, D. Shi, Y. Guo, M. Li, X. Zhou, Q. Huang, S. Du, The development of cladding materials for the accident tolerant fuel system from the Materials Genome Initiative, Scr. Mater. 141 (2017) 99–106, doi:10.1016/j.scriptamat.2017.07.030.

[22] J.R. ed. Rumble, CRC Handbook of Chemistry and Physics, 103rd ed., CRC Press/Taylor & Francis, Boca Raton, FL, 2021.

[23] B.A. Pint, Performance of FeCrAl for accident-tolerant fuel cladding in high-temperature steam, Corros. Rev. 35 (2017) 167–175, doi:10.1515/corrrev-2016-0067.

[24] B.A. Pint, K.A. Unocic, K.A. Terrani, Effect of steam on high temperature oxidation behaviour of alumina-forming alloys, Mater. High Temp. 32 (2015) 28–35, doi:10.1179/0960340914Z.00000000058.

[25] C. Tang, A. Jianu, M. Steinbrück, M. Grosse, A. Weisenburger, H.J. Seifert, Influence of composition and heating schedules on compatibility of FeCrAl alloys with high-temperature steam, J. Nuclear Mater. 511 (2018) 496–507, doi:10.1016/j.jnucmat.2018.09.026.

[26] C. Kim, C. Tang, M. Grosse, Y. Maeng, C. Jang, M. Steinbrück, Oxidation mechanism and kinetics of nuclear-grade FeCrAl alloys in the temperature range of 500–1500°C in steam, J. Nuclear Mater. 564 (2022) 153696, doi:10.1016/j.jnucmat.2022.153696.

[27] B. Qiu, J. Wang, Y. Deng, M. Wang, Y. Wu, S.Z. Qiu, A review on thermohydraulic and mechanical-physical properties of SiC, FeCrAl and Ti_3SiC_2 for ATF cladding, Nuclear Eng. Technol. 52 (2020) 1–13, doi:10.1016/j.net.2019.07.030.

[28] J.W. McMurray, R. Hu, S.V Ushakov, D. Shin, B.A. Pint, K.A. Terrani, A. Navrotsky, Solid-liquid phase equilibria of Fe-Cr-Al alloys and spinels, J. Nuclear Mater. 492 (2017) 128–133, doi:10.1016/j.jnucmat.2017.05.016.

[29] P. Pacenti, F. Toci, R. Nannicini, R.A.H. Edwards, U. Montaretto, M. della Rose, G. Buscaglia, Dissolution of UO2 by FeO melts. Project CIT (Corium Interactions and Thermochemistry) EU Report EUR 18661 EN, 1998. Dissolution of UO2 by FeO melts. Project CIT (Corium Interactions and Thermochemistry) (accessed October 26, 2022).

[30] T. Amano, High-temperature oxidation of FeCrAl(Y, Pt) alloys in oxygen–water vapour, Mater. High Temp. 28 (2011) 342–348 doi:10.3184/096034011×13190156331030.

[31] S.V. Bechta, E.V. Krushinov, V.I. Almjashev, S.A. Vitol, L.P. Mezentseva, Yu.B. Petrov, D.B. Lopukh, V.B. Khabensky, M. Barrachin, S. Hellmann, K. Froment, M. Fischer, W. Tromm, D. Bottomley, F. Defoort, V.V. Gusarov, Phase diagram of the ZrO_2–FeO system, J. Nuclear Mater. 348 (2006) 114–121, doi:10.1016/j.jnucmat.2005.09.009.